ACS APPLIED MATERIALS & INTERFACES

www.acsami.org Research Article

Carbon Nanotube Based Robust and Flexible Solid-State Supercapacitor

Thushani De Silva, Cole Damery, Rana Alkhaldi, Robinson Karunanithy, Dinuka H. Gallaba, Prasanna D. Patil, Milinda Wasala, Poopalasingam Sivakumar, Aldo Migone, and Saikat Talapatra*

Cite This: *ACS Appl. Mater. Interfaces* 2021, 13, 56004–56013 Read Online

ACCESS | Metrics & More | Article Recommendations | Supporting Information

ABSTRACT: All solid-state flexible electrochemical double-layer capacitors (EDLCs) are crucial for providing energy options in a variety of applications, ranging from wearable electronics to bendable micro/nanotechnology. Here, we report on the development of robust EDLCs using aligned multiwalled carbon nanotubes (MWCNTs) grown directly on thin metal foils embedded in a poly(vinyl alcohol)/phosphoric acid (PVA/H_3PO_4) polymer gel. The thin metal substrate holding the aligned MWCNT assembly provides mechanical robustness and the PVA/H_3PO_4 polymer gel, functioning both as the electrolyte as well as the separator, provides sufficient structural flexibility, without any loss of charge storage capacity under flexed conditions. The performance stability of these devices was verified by testing them under straight and bent formations. A high value of the areal specific capacitance (C_{SP}) of ~14.5 mF cm^{-2} with an energy density of ~1 μW h cm^{-2} can be obtained in these devices. These values are significantly higher (in some cases, orders of magnitude) than several graphene as well as single-walled nanotube-based EDLC's utilizing similar electrolytes. We further show that these devices can withstand multiple (~2500) mechanical bending cycles, without losing their energy storage capacities and are functional within the temperature range of 20 to 70 °C. Several strategies for enhancing the capacitive charge storage, such as physically stacking (in parallel) individual devices, or postproduction thermal annealing of electrodes, are also demonstrated. These findings demonstrated in this article provide tremendous impetus toward the realization of robust, stackable, and flexible all solid-state supercapacitors.

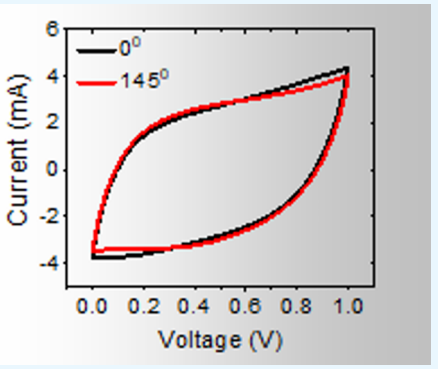

KEYWORDS: *carbon nanotubes, solid-state supercapacitor, electrochemical double layer, polymer gel electrolyte, charge storage*

INTRODUCTION

The increasing demand for energy and the limitations in accessibility for power sources have motivated us to seek better energy storage systems.[1,2] While batteries serve as adequate energy storage devices with high energy density, capacitors have their own place due to the high-power density.[3] However, there is an increasing focus on supercapacitors (SCs) as better energy storage devices because they match up the gap between a battery and a conventional capacitor.[4] Apart from that, SCs typically possess high specific capacitance (C_{SP}) compared to a conventional capacitor.[5] There are two types of energy storage mechanisms that could occur in a SC, electrical double-layer capacitances (EDLCs) and pseudo-capacitance.[6,7] EDLC is governed by the formation of the double layer between the electrode surface and the electrolyte due to the accumulation of charges.[8] Pseudo-capacitance is facilitated by the fast and reversible redox reactions which occur on the surface of electrodes. A capacitor which utilizes both mechanisms is categorized as a hybrid capacitor.[1] In both cases, the surface area of the electrode material of an EDLC, therefore, plays an important role because it can be generally said that the higher the surface area, the higher the capacitance will be.[9] This has motivated the usage of nanomaterials such as SC electrodes due to their large specific surface area (SSA).[10] Particularly, carbon-based nanomaterials such as activated carbon, carbon nanofibers, mesoporous carbon, diamond-like carbon, carbon nanotubes (CNTs), graphene, and carbide-derived carbon are used widely.[1,11,12]

With the emergence of flexible and portable devices, attention on flexible SCs has increased due to their numerous applications in wearable electronics, smart garments, and so forth.[13−15] The popular strategies that are adhered to achieve the flexibility of a SC are either fabricating flexible free-standing films of the active materials or supporting active materials on flexible substrates.[16] In recent years, flexible substrates, such as Bucky papers, flexible graphene paper, polyester−cotton fabrics, and so forth, are employed to

Received: July 3, 2021
Accepted: October 12, 2021
Published: November 18, 2021

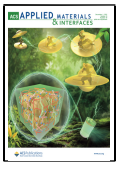

https://doi.org/10.1021/acsami.1c12551
ACS Appl. Mater. Interfaces 2021, 13, 56004–56013

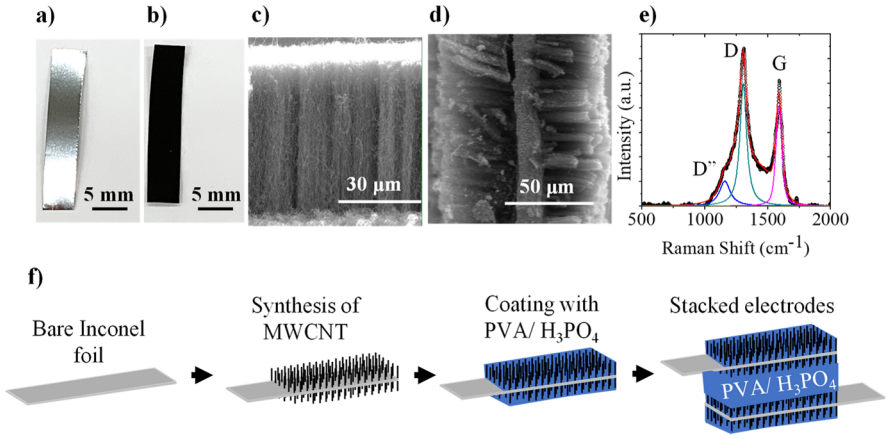

Figure 1. (a) Bare Inconel foil, (b) as-synthesized MWCNT on an Inconel substrate, (c) SEM image of the vertically aligned MWCNT forest on the Inconel strip, (d) SEM Image of the MWCNT showing the growth on both sides of the Inconel substrate, (e) Raman spectrum of the MWCNT, and (f) fabrication process.

fabricate solid-state SCs. Non-conducting or conducting polymer composites, such as polyaniline (PANI) mixed with various nanomaterials, are widely used as well.[1,17] When achieving the flexible, foldable, stretchable, or twistable nature in a SC electrode, supporting active materials on flexible substrates or developing polymer composites have their own advantages.[18,19] However, there are several challenges present during the development of polymer composites, such as controllable mixing/compounding, stabilization of the dispersion, and orientation of the dispersed phase, and so forth. Also, the uniformity of the dispersion of the nanomaterial in a polymer is compromised by the formation of agglomerates.[20] Apart from this, typical CNT-based polymer composites or Bucky papers tend to arrange the tubes in a randomly entangled manner, decreasing the effective accessible surface area.[21] On the other hand, fabricating vertically aligned CNTs on a flexible substrate could help to achieve a higher SSA for the diffusion of electrolytes and a better structure.[21,22] When choosing a flexible substrate (which will be the current collector) to directly synthesize CNTs for SC application, one of the key features is good electrical conductivity. This has attracted the notion of employing thin metal foils as substrates for depositing electrode materials for SC because thin metal foils are robust, flexible, and are a good conductor of electricity.[23] This has led to the synthesis of CNTs on metal substrates such as aluminum, stainless steel, Fe−Ni-based metal alloy foils, and so forth.[16,22,24,25] However, most of the past works on the synthesis of CNT on metal foils require the deposition of the catalyst and pre-treatments,[22] adding process steps for developing a SC electrode. In the past, it was shown that it is possible to grow CNTs directly on specific metal alloys via a single-step process of chemical vapor deposition (CVD).[26,27] Here, we show the possibility of fabricating an all solid-state SC by using vertically aligned multiwall CNTs (MWCNTs) directly synthesized on as received thin Inconel 600 foil (Inconel) purchased from Goodfellow corporation. Inconel is a superalloy which possesses a tensile strength of 600−1200 MPa and has an electrical resistivity around 103 $\mu\Omega$ cm (as reported by the manufacturer). The MWCNT has been synthesized via the CVD technique. Poly(vinyl alcohol)/phosphoric acid (PVA/H_3PO_4) polymer gel electrolyte was coated on the MWNTs grown on the metal foils. The PVA/H_3PO_4 polymer gel functions both as the electrolyte as well as the separator, and it provides sufficient structural flexibility. Multiple devices were fabricated and tested where the highest areal specific capacitance (C_{SP}) was found to be ∼14.5 mF cm^{-2} at 1 mV s^{-1} with an energy density of ∼1 μW h cm^{-2}. These values are significantly higher (in some cases orders of magnitude) than several graphene as well as single-walled nanotube-based EDLC's utilizing a similar electrolyte.[18,28]

The performance stability of these devices was verified by undertaking relevant electrochemical measurements under straight and bent forms. We also demonstrate that these devices can withstand several (∼2500) mechanical bending cycles, without losing their energy storage capacity. Because these EDLCs are free standing monoliths, a simple strategy of stacking individual devices allowed us to enhance the capacitive charge storage ability. Further, a device fabricated utilizing MWCNTs shows a significant enhancement (∼61% at 5 mV s^{-1}) of the capacitive storage ability, after postproduction annealing in air.

EXPERIMENTAL METHODS

Synthesis of MWCNT on Inconel. The CVD process is commonly used to deposit a wide range of materials, including CNTs.[29] The thermal CVD method used in this study is an air-assisted technique that utilizes a mixture of ferrocene and xylene as the precursor.[26,30] Following the process of previous works on synthesizing MWCNT on Inconel, we were able to grow aligned MWCNT on thin Inconel foils that had a thickness of 12.5 μm.[26,30] The optimal growing parameters for the synthesis process were that the optimal temperature was around 770 °C, and the optimal region was from 26 to 30 cm with respect to the oven entrance. For postproduction annealing, a tube furnace was used. The sample was annealed at 300 °C in air for 1 h.

The results of the MWCNT/Inconel electrode growth, and the schematics of the process followed to fabricate flexible SCs are shown in Figure 1. Figure 1a,b presents optical images of bare Inconel foil and as-synthesized MWCNT on Inconel, which has completely coated its surface. The aligned structure of the MWCNT forest is evident in Figure 1c. Because the Inconel stripes were used in their pristine condition, the nature of the synthesis allows MWCNT to grow on both sides of Inconel foil, as illustrated in Figure 1d.

Raman Characterization. The as-produced samples were analyzed using Raman spectroscopy measurement. Raman spectroscopy is a powerful nondestructive material characterization technique, which has been widely employed for studying MWCNT. The Raman spectrum of the sample was acquired using iHR 550 (HORIBA Scientific). The excitation wavelength of the Raman spectrometer is

https://doi.org/10.1021/acsami.1c12551
ACS Appl. Mater. Interfaces 2021, 13, 56004−56013

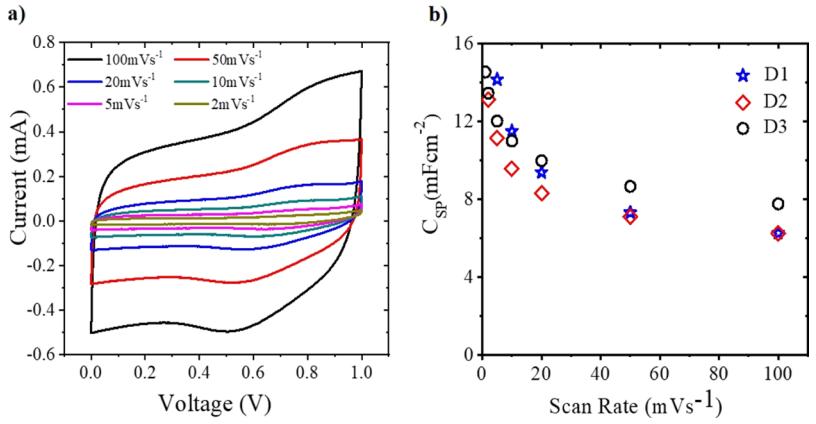

Figure 2. (a) CV measurements performed at different scan rates on D3 is presented and (b) variation of specific capacitance with a scan rate for three different devices are shown.

785 nm, and it is equipped with an Olympus BX 41 microscope with 10×, 50×, and 100× magnification objectives. A 600 grooves mm^{-1} grating was utilized with laser power at ∼12 mW to acquire the data. The Raman spectrum obtained for as-synthesized nanotube forest on the Inconel substrate, indicating the positions of D and G bands (at 1305.35 and 1589.30 cm^{-1}) as well as the D″ band (at 1160.0 cm^{-1})[31,32] is shown in Figure 1e. While the G band corresponds to the graphitic like in-plane mode, the D band occurs due to the disorder in the honeycomb lattice of the MWCNT walls.[33] The relative intensity of the D band with respect to the G band (I_D/I_G) is a good measure of the quality of CNTs.[34] The I_D/I_G calculated for the Inconel samples with the optimized MWCNT growing conditions was 1.23. For high-quality nanotubes, the Raman intensity of the G band is greater than the D band. However, these intensities also depend on the laser excitation photon energy (E_{laser}),[35] where the D band's intensity increases with the decrease of E_{laser} and the I_D/I_G ratio tends to have a higher value for the 785 nm wavelength comparatively.[36,37] Another factor that affects the I_D/I_G ratio of the MWCNT is the substrate it has been synthesized on. A previous study has displayed a higher I_D/I_G ratio for MWCNTs synthesized on stainless steel.[24] The disorder vibrations of MWCNTs on the Inconel substrate could be more intense than the ordered vibrations so that the I_D/I_G ratio appears to be high. The 2D mode (not shown) that appears at the far end is the second-order overtone mode, and in principle its intensity does not depend on the presence of disorders.[31]

SSA Characterization. The SSA of a material is one of the key factors to assess its suitability for applications (such as sensors, catalysts, battery and SC electrode, etc.) because it is an indication of the material's activity and adsorption capacity.[38] Here, we have assessed the SSA of the MWCNT using the volumetric gas adsorption isotherm[39] (Supporting Information). SSA of the MWCNT synthesized on Inconel was estimated to be ∼30 $m^2\ g^{-1}$.

SC Device Fabrication Process. The fabrication process steps for assembling the SC devices are illustrated in Figure 1f. First, the Inconel foil was cut into 5 mm by 25 mm rectangular strips. Then, the MWCNTs were synthesized, employing the optimized parameters mentioned above. Next, one end of these strips (∼5 mm along the long edge) was cleared of the nanotubes and masked to be protected during the coating of the polymer electrolyte (so that this end can serve as the electrical connection point of the current collector thus formed).

In the case of flexible SCs, a polymer electrolyte is more suitable than a liquid electrolyte because it rules out the necessity of a robust encapsulation to prevent leakage. The SC in this study has been fabricated using a non-conducting polymer gel made of polyvinyl alcohol and phosphoric acid (PVA/H_3PO_4), which serves as both the electrolyte and the separator. This polymer gel also prevents any potential leakage because the electrolyte is bound within the polymer matrix.[40] The PVA/H_3PO_4 polymer electrolyte was prepared by mixing the PVA powder with water (1 g of PVA/10 mL of H_2O) and concentrated phosphoric acid (0.8 g).[40] Fist, water was heated up to ∼90 °C and then 1 g of PVA (98−99% hydrolyzed, medium molecular weight, Alfa Aesar) powder was added to it under stirring. Once the solution became clear, it was removed from heat and left to cool down. After cooling down, 0.8 g of concentrated phosphoric acid was added and stirred thoroughly to obtain a viscous solution. Then, the partially masked Inconel strips (from the previous step) were dip coated in the polymer electrolyte and left to air-dry overnight. It is important to cover the surface (apart from the masked area) of the electrodes entirely with the polymer in order to avoid a short-circuit (with the electrode on top) when obtaining the SC architecture. Once the electrodes were dried completely overnight, the two ends that serve as the current collector were unmasked and cleaned using acetone. Then, they were placed on top of each other by applying another coating of the polymer gel in the middle. To achieve a thinner and uniform middle polymer layer, a pressure of 940.8 kPa was applied over the electrodes and was left to dry under this applied pressure for 3 days before performing the electrochemical characterization.

RESULTS AND DISCUSSION

We have tested five different devices. Three SC devices, namely, D1, D2, and D3, were prepared using the method mentioned under the Experimental Section above, and utilized for basic electrochemical measurements. Detailed measurements in order to demonstrate the flexibility and robustness were performed on devices D1 and D3. D4 was fabricated using MWNCT/Inconel electrodes, which underwent a postproduction annealing. Another device, D5, was utilized to test the variation of the specific capacitance as a function of temperature T (20 °C < T < 70 °C).

The devices were initially tested by performing cyclic voltammogram (CV) measurements, galvanostatic charge−discharge (GCD) measurements, and electrochemical impedance spectroscopy (EIS) measurements to assess their electrochemical properties. The measurements were carried out in the two-electrode system arrangement using a PARSTAT 2263 Advanced Electrochemical System. For the CV curves, the areal specific capacitance (C_{SP}) was measured using the following equation.

$$C_{SP} = \frac{\int I\, dV}{A \times \gamma \times \Delta V}$$

where $\int I\, dV$ is the area of the CV curve, γ is the scan rate, ΔV is the voltage window, and A is the area per electrode.[41] These results are shown in Figure 2.

https://doi.org/10.1021/acsami.1c12551
ACS Appl. Mater. Interfaces 2021, 13, 56004−56013

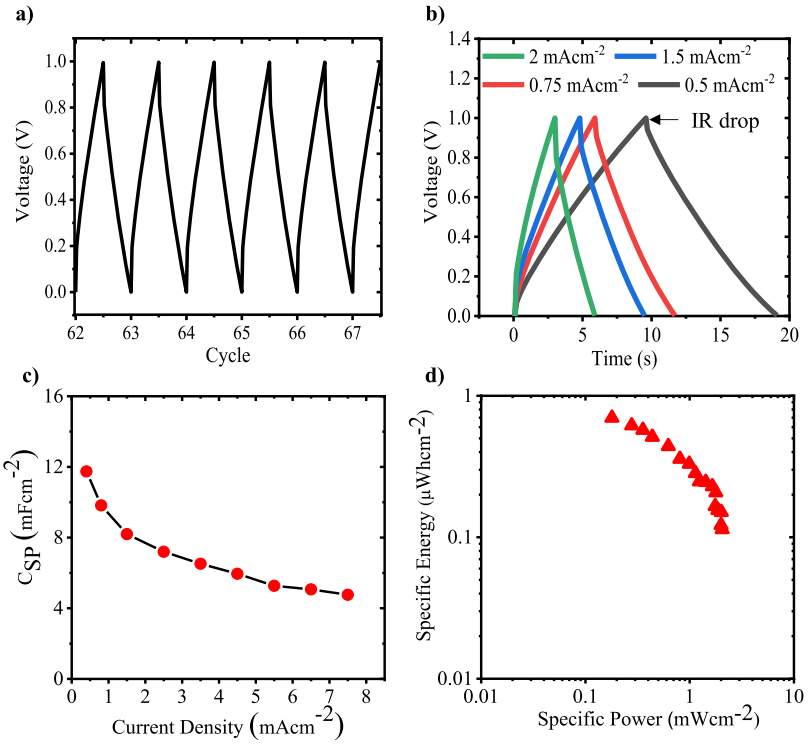

Figure 3. GCD measurements for SC (a) normalized GCD plot for D3, (b) variation of the normalized GCD curve with the current density for D3, (c) variation of the C_{SP} with the current density for D3, and (d) areal Ragone plot of D3.

Figure 2a illustrates the CV curves obtained for D3 for different scan rates. The voltage window for PVA/H_3PO_4 was kept at 1 V.[40] The highest measured C_{SP} for D3 at 1 mV s^{-1} was found to be 14.5 mF cm^{-2}. These values are significantly higher than those of several previously reported flexible SC devices using the same or a similar electrolyte (e.g., areal C_{SP} of 0.552 mF cm^{-2} reported for single-walled CNT-based SC employing PVA/H_3PO_4 polymer electrolyte[28] and a 0.6 mF cm^{-2} areal C_{SP} at 100 mV s^{-1} reported for CNT-based SC with a PVA/KOH polymer electrolyte[19]). A tabulation of areal C_{SP} values as well as other performance parameters for some of these devices from past reports is also presented in Table S1 (Supporting Information).

Typically, based on the rectangular shape of the CV curves, which displays a good reversibility, one can conclude that the charge storage mechanism could be dominated by the formation of a pure electrochemical double layer.[42] However, in our measurements, although we have a near rectangular CV response, we also observe a redox peak, which could be due to the contribution from pseudo-capacitance.[42] The quasi-rectangular shape of the CV curve further confirms that both EDLC and some contribution from pseudo-capacitance are present in our devices.[43] The percentage of EDLC and pseudo-capacitance present in the SC was estimated based on inner (q_{in}) and outer (q_{out}) charge contributions to the total capacitance (Supporting Information).[44] The percentage contribution from EDLC was estimated to be ∼64%, which is dominant compared to the ∼36% contribution from the pseudo-capacitance. It is possible for EDLC with high-area carbon electrodes to exhibit pseudo-capacitance due to the presence of amorphous carbon, defects on the electrode surface, and oxygen containing functional groups.[45−47] It has been reported that the D band in the Raman spectrum of CNTs is attributable to the presence of the disordered amorphous carbon on the tube side-wall, rather than defects in the tube wall itself.[48] Therefore, the presence of a strong D band in the Raman spectrum illustrated on Figure 1e indicates that the MWCNT grown on Inconel could contain a significant amount of amorphous carbon, which possibly has given rise to the considerable amount of pseudo-capacitance. The D band can also correspond to other MWCNT defects such as grain boundaries, which could increase the defects on the electrode surface and further enhance the pseudo-capacitive behavior.[48,49] A literature that has used a similar fabrication process with carbon-based electrodes has shown the appearance of redox peaks on CV curves for electrolytes, such as PVA/H_2SO_4 and so forth.[50] Due to the nature of the PVA gel polymer coating on the electrodes, it is possible that the polymer is not able to completely penetrate through to the material, hence, leaving voids and pores within the electrode. Specifically, in this case, where the electrode is a vertically aligned MWCNT forest, and the electrolyte was introduced starting from the top of the surface. This could potentially leave many voids and pores inside the nanotube forest. The pseudo-capacitive mechanism often benefits from these voids, pores, crevices, cracks, and so forth,[44] and hence can increase the contribution from pseudo-capacitance. Another possible source of pseudo-capacitance is the adsorption of ions onto the electrode.[41,51]

From the results presented in Figure 2a, it can be observed that the position of the redox peak shifts with the scan rate, which is perhaps more prominent during the reverse sweep; hence, the redox peak potential is scan rate dependent. This shows that the nature of these redox reactions are irreversible.[52] Figure 1b illustrates the dependence of C_{SP} as a function of the scan rate for D1, D2, and D3. The C_{SP} tends to decrease with the increasing scan rate, a typical behavior of porous electrodes employed for EDLC and is mostly attributed

https://doi.org/10.1021/acsami.1c12551
ACS Appl. Mater. Interfaces 2021, 13, 56004−56013

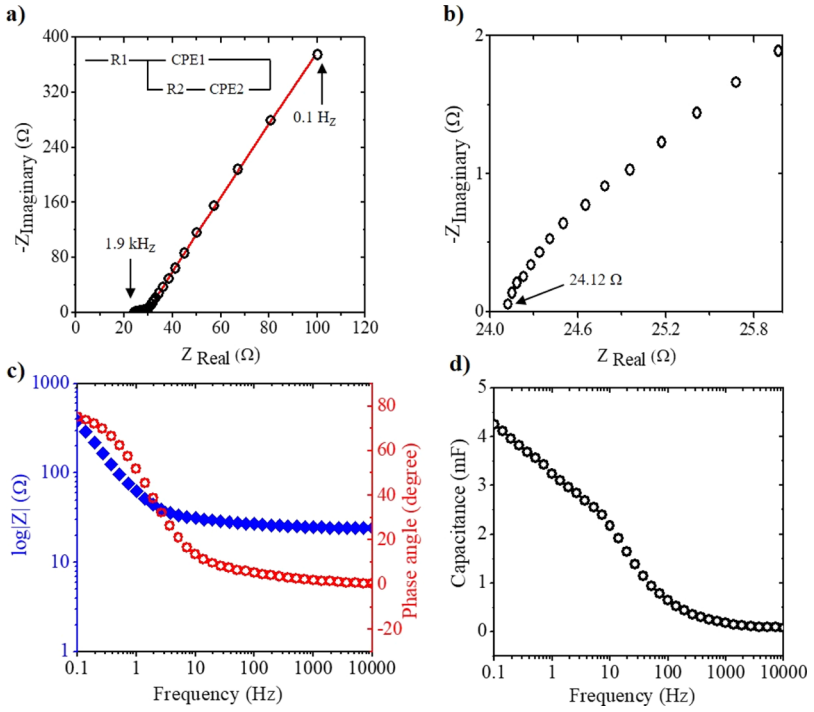

Figure 4. Impedance spectrum analysis for D3 (a) Nyquist plot, (b) high-frequency region of the Nyquist plot showing the intercept of Z_{real}, (c) Bode impedance and phase-angle plots, and (d) capacitance response with the frequency.

to the insufficient time for the electrolyte ions to diffuse into or adsorb out of the inner pores of MWCNT,[53] under extremely fast scan rates.

GCD cycles were also performed on all the devices. In Figure 3, we have presented the results obtained for D3. Figure 3a shows the normalized GCD curve obtained for D3, which has a triangular shape. This indicates that the charge storage mechanism in the SC is perhaps dominated by the formation of a double layer.[54] However, the GCD curves display an *IR* drop, related to the energy losses arising from the internal or equivalent series resistance (ESR).[55] The device capacitance from the GCD curve was measured using the equation $C = I/(dV/dt)$, where I is the discharge current and dV/dt is the calculated from the slope of the GCD discharge curve.[56] The areal C_{SP} for GCD was calculated using $C_{SP} = 2 \times C/A$, where A is the area per electrode. The values obtained are similar to the C_{SP} values obtained from the CV curves.[57] Variation of the normalized GCD curve with different current densities is illustrated in Figure 3b, where the current density increases from right to left. Because the *IR* drop increases with increasing discharge current, the C_{SP} typically decreases, which is evident in Figure 3c.[55] Figure 3d illustrates the variation of the areal specific power density versus areal specific energy (also known as the Ragone plot) for D3. The Ragone plot is typically used to evaluate the performance of an electrochemical energy storage device.[58] The Ragone plot of D3 shows that the performance of the device presented in this work is within the range of SC.[15] Similar values have been reported for a flexible three-dimensional porous graphene foam-based SC, where the power and energy densities are reported to be 0.27 mW cm^{-2} and 3.4 μW h cm^{-2}, respectively.[15] Another work on the graphene thin film-based SC, employing gel polymer electrolyte, has reported a power and energy density of 0.106 mW cm^{-2} and 0.235 μW h cm^{-2}, respectively.[50]

In order to further characterize the performance of the EDLC device and to model the equivalent circuitry that is in effect under the operating conditions of the device, we have performed EIS measurements. The knowledge of the equivalent circuit can be used to extract important physical parameters such as the ESR of the device under test. The impedance spectrum for D3 was obtained for the frequency ranging from 1.9 kHz to 100 mHz. The resulting Nyquist plot is shown in Figure 4a. Figure 4b shows the high-frequency response of the Nyquist plot illustrating an *x*-axis intercept of 24.12 Ω. The inset in Figure 4a displays the equivalent circuit model used to fit the impedance spectrum obtained for the device. From the Nyquist plot and the fitted model, the ESR of the device, R_1, was found to be 24.4 Ω. We believe that the ESR in these devices are mostly due to the electrical resistances of the PVA/H_3PO_4 electrolyte and charge-transfer barrier between the MWCNT and the Inconel sheet. The constant-phase elements (CPEs) typically indicate non-ideal capacitive behavior and represent systems with the surface disorder of the electrode material, electrode porosity, and electrolyte adsorption processes.[41,59]

The capacitance from the CPE was calculated using the equation $C = P/[f^{1-n} \times \sin(n\pi/2)]$, where P and n are the fitting parameters for CPE components and f is the lowest frequency value used for acquiring the impedance spectrum.[41] Some key values obtained from the fitting are presented in Table 1. The values obtained from the fitting can also provide some key insights into the capacitive behavior occurring at the electrodes. The value of n illustrates how good the capacitive behavior is, where $n = 1$ gives ideal capacitive behavior.[59] From Table 1, it can be seen that the fitting parameters n_1 and n_2 are much closer to 1, which further confirms the good capacitive behavior of the device. The second CPE component present in the circuit (CPE2 which is parallel to CPE1) is added in order

https://doi.org/10.1021/acsami.1c12551
ACS Appl. Mater. Interfaces 2021, 13, 56004−56013

Table 1. Impedance Spectra Fitting Parameters

circuit components	straight EDLC (0°)	bent EDLC (145°)
R_1 (ESR) (Ω)	24.4	24.2
R_2 (Ω)	1.64	1.55
P_1	0.0012	0.0013
n_1	0.81	0.78
P_2	0.0026	0.0021
n_2	0.92	0.93
CPE1 (F)	0.0020	0.0024
CPE2 (F)	0.0034	0.0025
total capacitance (F)	0.0054	0.0049
experimental (F)	0.0052 at 20 mV s^{-1}	0.0052 at 20 mV s^{-1}

to model the possible contribution from the pseudocapacitance.[51,59]

A pure capacitive behavior should display a vertical line in the Nyquist plot, which only contains an imaginary impedance.[60,61] However, the Nyquist plot of D3 contains a slope at the low-frequency region and becomes a form of a semicircle at the high-frequency region. Typically, the appearance of the semicircle is due to the capacitive systems with leakage pathways. When modeling these types of systems, the semicircles could be accommodated by including a resistor parallel to the capacitor (here, it is the element denoted CPE1), enabling it to self-discharge.[51] Therefore, a resistive component denoted R_2 has been included parallel to the element CPE1.[62] The resistance R_2 at the high-frequency range can be attributed to the internal charge-transfer barrier[41] (as manifested through the partial semicircle behavior seen in the Nyquist plot). A value of 1.64 Ω was obtained for this parameter through the fitting. Therefore, there exists some resistance arising from the charge-transfer barrier in the polymer electrolyte; although, a graphene-based SC utilizing a PVA/H_3PO_4 polymer electrolyte has reported the absence of a semicircle region, indicating low faradaic resistances in the electrolyte.[63] From the fitting, the 0° angle C_{SP} obtained for D3 was found to be 0.0054 F, which is comparable to a value of ∼0.0052, obtained from the CV (at 20 mV s^{-1} scan rate) and GCD (at 0.6 mA cm^{-2} current density) measurements. The Bode plot in Figure 4c clearly shows the capacitive behavior of the device, where the impedance tends to decrease linearly with the increase of frequency at the low-frequency range due to ion diffusion.[17] At the high-frequency range, impedance becomes almost constant due to the charge-transfer effects and R_2 because the electrolyte and the material resistance dominantly define the device performance.[15] Further, the phase shift is relatively close to 90° in the lower frequency region (indicating a steeper slope), which confirms a good capacitive behavior for the device.[64] Figure 4d illustrates how the device capacitance decreases with the increase of the frequency.

In order to justify the choice of thin Inconel foils for flexible and bendable EDLC electrode application, electrochemical measurements were performed on these devices under different bend angles as well as after repetitive mechanical bending cycles. Initial electrochemical measurements were performed for the bent arrangement with a maximum tested bending angle at 145°. These results are presented in Figure 5. Figure 5a illustrates the CV curves obtained for D3, under a bend angle of 145° and at 0° at 10 mV s^{-1}. An optical image of the SC under bend conditions is included in the inset of Figure 5b. Overall, the 0 and 145° C_{SP} seems to vary at each scan rate, as is evident in Figure 5b, and the largest variation was

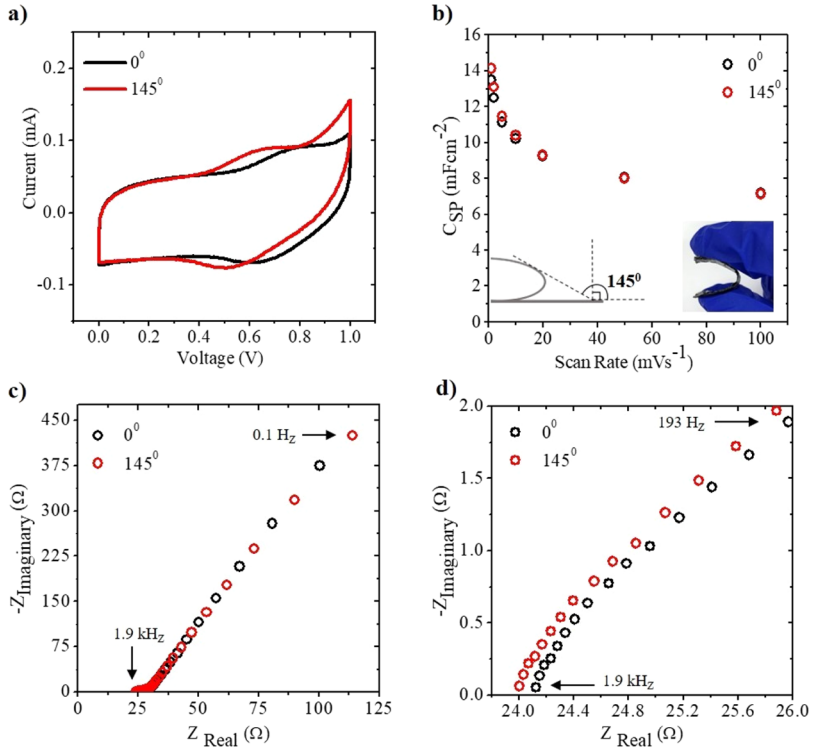

Figure 5. Bending testing for D3 (a) CV curves for the straight and bent arrangement at a scan rate of 10 mV s^{-1} and (b) variation of the C_{SP} with the scan rate at 0° angle and tested maximum bend angle of 145°. (Inset) EDLC under bending conditions. (c) Nyquist plot for 0° angle and 145° and (d) high-frequency region of the Nyquist plot is shown.

https://doi.org/10.1021/acsami.1c12551
ACS Appl. Mater. Interfaces 2021, 13, 56004−56013

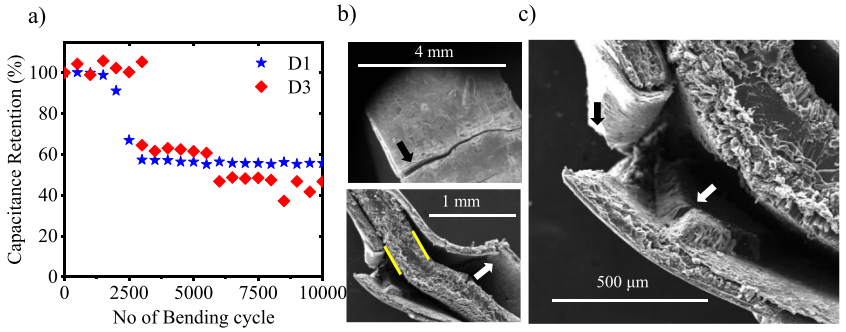

Figure 6. (a) Percentage change in C_{SP} as a function of mechanical bending cycles for D1 and D3 are presented. (b) (Top) SEM image of the top surface of the electrode showing a crack (black arrow) on the top surface of the device D3 and (bottom) peeled of the MWCNT/electrolyte assembly (white arrow) from the middle PVA/H_3PO_4 electrolyte layer, indicated by the parallel lines. (c) SEM image obtained at a higher magnification for the portion of the region shown in the bottom panel of (b). The black and white arrows show the broken metal backbone and peeled MWCNT/electrolyte assembly, respectively.

observed at 1 mV s^{-1}. At 100 mV s^{-1}, the bent C_{SP} was 0.83% less than the 0° C_{SP}. In contrast, at 1 mV s^{-1}, the bent C_{SP} was 4.51% greater than the straight C_{SP}. Furthermore, as seen in Figure 5a, the peaks on the CV curve at the bent position (along both charge and discharge paths) have shifted toward the left side of the graph. Bending of the device could potentially change the initial morphology of the aligned MWCNT up to some extent (momentarily).[22] This could lead to the electrolyte being in contact with more/different defect sites or amorphous carbon on MWCNT walls at the bent position, hence induced a change in the overall oxidization state compared to the initial position, which has driven the pseudo-capacitive peaks toward the left side.

The impedance spectroscopy response obtained for the 145° bend angle with respect to the 0° angle is illustrated in Figure 5c,d. The EIS data were fitted using the same equivalent circuit. The capacitance evaluated from the impedance spectrum for 145° angle is 0.0049 F, which only shows a variation of ∼9% from the 0° angle. The ESR at 145° was measured to be 24.2 Ω, which is similar to the ESR obtained at 0°. The values obtained from the EIS fitting is presented in Table 1.

To investigate the robustness of the fabricated devices, a mechanical bending test was performed where the devices were bent from 0° angle to 145° angle at a rate of about 60 cycles per min. The bending cycles were performed manually. The results from the mechanical bending cycles are presented in Figure 6. Figure 6a shows the percentage change of the C_{SP} with the number of bending cycles taken for D1 and D3 for ∼10 000 bending cycles. Both devices seem to retain the initial capacitance until ∼2500 bending cycles. Thereafter, the device capacitance reduces by ∼45−50% of its original capacity for both the devices tested. A somewhat similar behavior has been reported for the SC made of the MWCNT directly synthesized on aluminum foil, where the capacitance was retained (and eventually improves) until the first 2000 bending cycles; thereafter, the foil gets deformed.[22] Another SC constructed with a combination of PANI/CNTs/Au/polyethylene terephthalate shows a good capacitive retention up until 100 bending cycles.[65]

For the devices presented in this article, continual bending, and further testing after the decrease of capacitance around 2500 bending cycles showed that the devices seem to retain about ∼50% of the original C_{SP} values. Scanning electron microscopy (SEM) investigation of the electrodes after 10 000 bending cycles was performed. The results are presented in Figure 6b,c. From the SEM images, we can conclude that the sharp reduction in the capacitance values after ∼2500 cycles of the bending test could be due to the cracking and peeling of the MWNCT/electrolyte assembly. From Figure 6b (bottom panel) and 6c, it can be seen that the middle layer of the PVA/H_3PO_4 electrolyte seems to be intact, while the two Inconel sheets at the top and the bottom have peeled off (white arrows in Figure 6). Thereafter, the portion of the complete EDLC assembly that was still intact is responsible for the sustained C_{SP} (∼50% value of the original capacitance). Similar cracking and peeling off of the active electrode material was also observed in the other device (D1) tested (Supporting Information, Figure S4).

Several other aspects as well as strategies for further improving the device performances were investigated (Supporting Information, Figure S5). For example, a preliminary investigation shows that these devices can be vertically stacked with ease to form robust assemblies in order to achieve higher capacitances (Figure S5a,b). The specific capacitances of the SC device can be improved significantly (Figure S5c,d) by using a postproduction annealed MWCNT/Inconel electrode and can function well within the temperature range of 20 to 70 °C (Figure S5e, f) (typical operational temperature expected for commercial applications), where the C_{SP} increases with the increasing temperature possibly due to a higher mobility of the electrolyte ions.[66,67]

CONCLUSIONS

This work presents a simple process for fabricating an all solid-state SC based on vertically aligned MWCNT directly synthesized on Inconel foil. The maximum observed areal capacitance is ∼14.5 mF cm^{-2}, which is calculated at 1 mV s^{-1} of scan rate for D3. Because the nature of the synthesis allows MWCNT to grow on both sides of the Inconel foil, the areal C_{SP} is higher compared to most of the similar work reported earlier. The device is fairly stable at straight and bent forms. While the direct synthesis of the MWCNT on metal foils should improve the charge transfer between the nanotubes and the current collector, the middle polymer layer, (with a typical thickness of ∼0.25 mm), increases the internal resistance. In fact, this is one of the key challenges in fabricating solid-state SCs because it is essential to have a middle polymer layer thick enough to prevent short-circuiting between the electrodes and thin enough to minimize the internal resistance. The usage of a

https://doi.org/10.1021/acsami.1c12551
ACS Appl. Mater. Interfaces 2021, 13, 56004−56013

metal foil as the substrate provides a strong structural backbone to the device but tends to limit its usage in rapid bending applications. The SC is stable up to 2500 bending cycles, where it fails, mainly due to the breaking of the metal foil. However, the capacitor still retains about 50% of its initial capacitance after the breaking of the Inconel foil. We also demonstrated that by annealing the as-synthesized Inconel stripes containing the CNTs, the C_{SP} of the devices can be further improved. This work is based on a reasonably simple fabrication process of all solid-state SC focused for applications in robust and flexible energy storage devices.

■ ASSOCIATED CONTENT

Supporting Information

The Supporting Information is available free of charge at https://pubs.acs.org/doi/10.1021/acsami.1c12551.

SSA measurement of the MWCNT synthesized on Inconel foil, comparison of the CV measurements of the SC with a device made of bare Inconel electrodes, tabulation of areal C_{SP} comparison with past work, information about electrode failure due to rapid bending, investigation on vertical stacking ability, effect of the postproduction annealing on the performance, variation of the C_{SP} with temperature, CV and GCD curves for D1 obtained at three different bent angles, and estimation of the EDLC and pseudo-capacitive contribution to the total capacitance (PDF)

Video showing the charging of the SC (MP4)

■ AUTHOR INFORMATION

Corresponding Author

Saikat Talapatra − *Department of Physics, Southern Illinois University, Carbondale, Illinois 62901, United States;* orcid.org/0000-0001-8503-7571; Email: saikat@siu.edu

Authors

Thushani De Silva − *Department of Physics, Southern Illinois University, Carbondale, Illinois 62901, United States;* orcid.org/0000-0002-5377-0952

Cole Damery − *Department of Physics, Southern Illinois University, Carbondale, Illinois 62901, United States*

Rana Alkhaldi − *Department of Physics, Southern Illinois University, Carbondale, Illinois 62901, United States*

Robinson Karunanithy − *Department of Physics, Southern Illinois University, Carbondale, Illinois 62901, United States*

Dinuka H. Gallaba − *Department of Physics, Southern Illinois University, Carbondale, Illinois 62901, United States*

Prasanna D. Patil − *Department of Physics, Southern Illinois University, Carbondale, Illinois 62901, United States;* orcid.org/0000-0002-9296-1102

Milinda Wasala − *Department of Physics, Southern Illinois University, Carbondale, Illinois 62901, United States;* orcid.org/0000-0003-1503-3756

Poopalasingam Sivakumar − *Department of Physics, Southern Illinois University, Carbondale, Illinois 62901, United States;* orcid.org/0000-0001-5250-9325

Aldo Migone − *Department of Physics, Southern Illinois University, Carbondale, Illinois 62901, United States*

Complete contact information is available at: https://pubs.acs.org/10.1021/acsami.1c12551

Author Contributions

S.T. supervised and designed the experiments. T.D.S., C.D., and R.A. synthesized the MWCNT. T.D.S. fabricated the devices and performed the electrochemical measurements and data analysis. R.K., T.D.S. and R.A. gathered and analyzed the Raman spectroscopy measurements. D.H.G. performed the SSA analysis. P.D.P. and M.W. performed the SEM imaging. All the authors discussed and contributed to the writing of the manuscript.

Notes

The authors declare no competing financial interest.

■ ACKNOWLEDGMENTS

The authors T.D.S. and S.T. would like to acknowledge the support by the APS Braslau Student Travel Award. Funding support for C.D. through NSF DMR and DoD Assure REU program (award #: 1757954) is also acknowledged. P.D.P. and M.W. acknowledges the support provided by the Southern Illinois University Carbondale, through Graduate School Doctoral Fellowship and College of Science Dissertation Research Award, respectively.

■ REFERENCES

(1) Chen, T.; Dai, L. Flexible Supercapacitors Based on Carbon Nanomaterials. *J. Mater. Chem.* **2014**, *2*, 10756−10775.

(2) Dong, S.; Li, Z.; Xing, Z.; Wu, X.; Ji, X.; Zhang, X. Novel Potassium-Ion Hybrid Capacitor Based on an Anode of K2Ti6O13 Microscaffolds. *ACS Appl. Mater. Interfaces* **2018**, *10*, 15542−15547.

(3) Lu, P.; Xue, D.; Yang, H.; Liu, Y. Supercapacitor and Nanoscale Research Towards Electrochemical Energy Storage. *Int. J. Smart Nano Mater.* **2013**, *4*, 2−26.

(4) Li, R.; Yang, Y.; Wu, D.; Li, K.; Qin, Y.; Tao, Y.; Kong, Y. Covalent Functionalization of Reduced Graphene Oxide Aerogels with Polyaniline for High Performance Supercapacitors. *Chem. Commun.* **2019**, *55*, 1738−1741.

(5) Chen, H.; Wang, G.; Chen, L.; Dai, B.; Yu, F. Three-Dimensional Honeycomb-Like Porous Carbon with Both Interconnected Hierarchical Porosity and Nitrogen Self-Doping from Cotton Seed Husk for Supercapacitor Electrode. *Nanomaterials* **2018**, *8*, 412.

(6) Wang, J.; Wang, C.; Gong, S.; Chen, Q. Enhancing the Capacitance of Battery-Type Hybrid Capacitors by Encapsulating MgO Nanoparticles in Porous Carbon as Reservoirs for OH−Ions from Electrolytes. *ACS Appl. Mater. Interfaces* **2019**, *11*, 21567−21577.

(7) Mitra, S.; Lokesh, K. S.; Sampath, S. Exfoliated Graphite−Ruthenium Oxide Composite Electrodes for Electrochemical Supercapacitors. *J. Power Sources* **2008**, *185*, 1544−1549.

(8) Shukla, A. K.; Sampath, S.; Vijayamohanan, K. Electrochemical Supercapacitors: Energy Storage Beyond Batteries. *Curr. Sci.* **2000**, *79*, 1656−1661.

(9) Vicentini, R.; Costa, L. H.; Nunes, W.; Vilas Boas, O.; Soares, D. M.; Alves, T. A.; Real, C.; Bueno, C.; Peterlevitz, A. C.; Zanin, H. Direct Growth of Mesoporous Carbon on Aluminum Foil for Supercapacitors Devices. *J. Mater. Sci.: Mater. Electron.* **2018**, *29*, 10573−10582.

(10) Li, S.; De Silva, T.; Arsano, I.; Gallaba, D.; Karunanithy, R.; Wasala, M.; Zhang, X.; Sivakumar, P.; Migone, A.; Tsige, M.; Ma, X.; Talapatra, S. High Adsorption of Benzoic Acid on Single Walled Carbon Nanotube Bundles. *Sci. Rep.* **2020**, *10*, 1−10.

(11) Xu, C.; Xu, B.; Gu, Y.; Xiong, Z.; Sun, J.; Zhao, X. S. Graphene-Based Electrodes for Electrochemical Energy Storage. *Energy Environ. Sci.* **2013**, *6*, 1388−1414.

(12) Mitra, S.; Sampath, S. Electrochemical Capacitors Based on Exfoliated Graphite Electrodes. *Electrochem. Solid-State Lett.* **2004**, *7*, A264.

(13) Liu, Y.-L.; Yan, C.; Wang, G.-G.; Zhang, H.-Y.; Dang, L.-Y.; Wu, B.-W.; Lin, Z.-Q.; An, X.-S.; Han, J.-C. Achieving Ultrahigh Capacity with Self-Assembled Ni (OH) 2 Nanosheet-Decorated Hierarchical Flower-like MnCo2O4. 5 Nanoneedles as Advanced Electrodes of Battery−Supercapacitor Hybrid Devices. *ACS Appl. Mater. Interfaces* **2019**, *11*, 9984−9993.
(14) Kumar, L.; Boruah, P. K.; Das, M. R.; Deka, S. Superbending (0−180°) and High-Voltage Operating Metal-Oxide-Based Flexible Supercapacitor. *ACS Appl. Mater. Interfaces* **2019**, *11*, 37665−37674.
(15) Manjakkal, L.; Núñez, C. G.; Dang, W.; Dahiya, R. Flexible Self-Charging Supercapacitor Based on Graphene-Ag-3D Graphene Foam Electrodes. *Nano Energy* **2018**, *51*, 604−612.
(16) Dubal, D. P.; Kim, J. G.; Kim, Y.; Holze, R.; Lokhande, C. D.; Kim, W. B. Supercapacitors Based on Flexible Substrates: an Overview. *Energy Technol.* **2014**, *2*, 325−341.
(17) Dubal, D. P.; Chodankar, N. R.; Kim, D.-H.; Gomez-Romero, P. Towards Flexible Solid-State Supercapacitors for Smart and Wearable Electronics. *Chem. Soc. Rev.* **2018**, *47*, 2065−2129.
(18) Xu, P.; Kang, J.; Choi, J.-B.; Suhr, J.; Yu, J.; Li, F.; Byun, J.-H.; Kim, B.-S.; Chou, T.-W. Laminated Ultrathin Chemical Vapor Deposition Graphene Films Based Stretchable and Transparent High-Rate Supercapacitor. *ACS Nano* **2014**, *8*, 9437−9445.
(19) Zhang, R.; Ding, J.; Liu, C.; Yang, E.-H. Highly Stretchable Supercapacitors Enabled by Interwoven CNTs Partially Embedded in PDMS. *ACS Appl. Energy Mater.* **2018**, *1*, 2048−2055.
(20) Julkapli, N. M.; Bagheri, S.; Sapuan, S. M. Multifunctionalized Carbon Nanotubes Polymer Composites: Properties and Applications. In *Eco-friendly Polymer Nanocomposites*; Springer, 2015; pp 155−214.
(21) Lu, W.; Dai, L. Carbon Nanotube Supercapacitors. In *Carbon Nanotubes*; IntechOpen, 2010.
(22) Dogru, I. B.; Durukan, M. B.; Turel, O.; Unalan, H. E. Flexible Supercapacitor Electrodes with Vertically Aligned Carbon Nanotubes Grown on Aluminum Foils. *Prog. Nat. Sci.: Mater. Int.* **2016**, *26*, 232−236.
(23) Vicentini, R.; Costa, L. H.; Nunes, W.; Vilas Boas, O.; Soares, D. M.; Alves, T. A.; Real, C.; Bueno, C.; Peterlevitz, A. C.; Zanin, H. Direct Growth of Mesoporous Carbon on Aluminum Foil for Supercapacitors Devices. *J. Mater. Sci.: Mater. Electron.* **2018**, *29*, 10573−10582.
(24) Lepró, X.; Lima, M. D.; Baughman, R. H. Spinnable Carbon Nanotube Forests Grown on Thin, Flexible Metallic Substrates. *Carbon* **2010**, *48*, 3621−3627.
(25) Seman, R. N. A. R.; Azam, M. A.; Mohamed, M. A. Highly Efficient Growth of Vertically Aligned Carbon Nanotubes on Fe−Ni Based Metal Alloy Foils for Supercapacitors. *Adv. Nat. Sci.: Nanosci. Nanotechnol.* **2016**, *7*, 045016.
(26) Talapatra, S.; Kar, S.; Pal, S. K.; Vajtai, R.; Ci, L.; Victor, P.; Shaijumon, M. M.; Kaur, S.; Nalamasu, O.; Ajayan, P. M. Direct Growth of Aligned Carbon Nanotubes on Bulk Metals. *Nat. Nanotechnol.* **2006**, *1*, 112−116.
(27) Pal, S. K.; Talapatra, S.; Kar, S.; Ci, L.; Vajtai, R.; Borca-Tasciuc, T.; Schadler, L. S.; Ajayan, P. M. Time and Temperature Dependence of Multi-Walled Carbon Nanotube Growth on Inconel 600. *Nanotechnology* **2008**, *19*, 045610.
(28) Kanninen, P.; Luong, N. D.; Sinh, L. H.; Anoshkin, I. V.; Tsapenko, A.; Seppälä, J.; Nasibulin, A. G.; Kallio, T. Transparent and Flexible High-Performance Supercapacitors Based on Single-Walled Carbon Nanotube Films. *Nanotechnology* **2016**, *27*, 235403.
(29) Gordon, R. Chemical Vapor Deposition of Coatings on Glass. *J. Non-Cryst. Solids* **1997**, *218*, 81−91.
(30) Shah, R.; Zhang, X.; Talapatra, S. Electrochemical Double Layer Capacitor Electrodes Using Aligned Carbon Nanotubes Grown Directly on Metals. *Nanotechnology* **2009**, *20*, 395202.
(31) Curran, S. A.; Talla, J. A.; Zhang, D.; Carroll, D. L. Defect-Induced Vibrational Response of Multi-Walled Carbon Nanotubes Using Resonance Raman Spectroscopy. *J. Mater. Res.* **2005**, *20*, 3368−3373.
(32) Wang, Y.; Alsmeyer, D. C.; McCreery, R. L. Raman Spectroscopy of Carbon Materials: Structural Basis of Observed Spectra. *Chem. Mater.* **1990**, *2*, 557−563.
(33) Zdrojek, M.; Gebicki, W.; Jastrzebski, C.; Melin, T.; Huczko, A. Studies of Multiwall Carbon Nanotubes Using Raman Spectroscopy and Atomic Force Microscopy. *Solid State Phenom.* **2004**, *99−100*, 265−268.
(34) Rao, R.; Reppert, J.; Podila, R.; Zhang, X.; Rao, A. M.; Talapatra, S.; Maruyama, B. Double Resonance Raman Study of Disorder in CVD-Grown Single-Walled Carbon Nanotubes. *Carbon* **2011**, *49*, 1318−1325.
(35) Pimenta, M. A.; Dresselhaus, G.; Dresselhaus, M. S.; Cançado, L. G.; Jorio, A.; Saito, R. Studying Disorder in Graphite-Based Aystems by Raman Spectroscopy. *Phys. Chem. Chem. Phys.* **2007**, *9*, 1276−1290.
(36) Sood, A. K.; Gupta, R.; Asher, S. A. Origin of the Unusual Dependence of Raman D Band on Excitation Wavelength in Graphite-Like Materials. *J. Appl. Phys.* **2001**, *90*, 4494−4497.
(37) Pimenta, M. A.; Jorio, A.; Brown, S. D. M.; Souza Filho, A. G.; Dresselhaus, G.; Hafner, J. H.; Lieber, C. M.; Saito, R.; Dresselhaus, M. S. Diameter Dependence of the Raman D-band in Isolated Single-Wall Carbon Nanotubes. *Phys. Rev. B: Condens. Matter Mater. Phys.* **2001**, *64*, 041401.
(38) Gadipelli, S.; Guo, Z. X. Graphene-Based materials: Synthesis and Gas Sorption, Storage and Separation. *Prog. Mater. Sci.* **2015**, *69*, 1−60.
(39) Volfkovich, Y. M.; Rychagov, A. Y.; Sosenkin, V. E.; Efimov, O. N.; Os'makov, M. I.; Seliverstov, A. F. Measuring the Specific Surface Area of Carbon Nanomaterials by Different Methods. *Russ. J. Electrochem.* **2014**, *50*, 1099−1101.
(40) Kaempgen, M.; Chan, C. K.; Ma, J.; Cui, Y.; Gruner, G. Printable Thin Film Supercapacitors Using Single-Walled Carbon Nanotubes. *Nano Lett.* **2009**, *9*, 1872−1876.
(41) Winchester, A.; Ghosh, S.; Feng, S.; Elias, A. L.; Mallouk, T.; Terrones, M.; Talapatra, S. Electrochemical Characterization of Liquid Phase Exfoliated Two-Dimensional Layers of Molybdenum Disulfide. *ACS Appl. Mater. Interfaces* **2014**, *6*, 2125−2130.
(42) Molinari, A.; Leufke, P. M.; Reitz, C.; Dasgupta, S.; Witte, R.; Kruk, R.; Hahn, H. Hybrid Supercapacitors for Reversible Control of Magnetism. *Nat. Commun.* **2017**, *8*, 15339.
(43) Senthilkumar, S. T.; Selvan, R. K.; Lee, Y. S.; Melo, J. S. Electric Double Layer Capacitor and Its Improved Specific Capacitance Using Redox Additive Electrolyte. *J. Mater. Chem. A* **2013**, *1*, 1086−1095.
(44) Pandit, B.; Dubal, D. P.; Gómez-Romero, P.; Kale, B. B.; Sankapal, B. R. V 2 O 5 Encapsulated MWCNTs in 2D Surface Architecture: Complete Solid-State Bendable Highly Stabilized Energy Efficient Supercapacitor Device. *Sci. Rep.* **2017**, *7*, 43430.
(45) Pan, H.; Li, J.; Feng, Y. P. Carbon Nanotubes for Supercapacitor. *Nanoscale Res. Lett.* **2010**, *5*, 654−668.
(46) Pandit, B.; Dubal, D. P.; Sankapal, B. R. Large Scale Flexible Solid State Symmetric Supercapacitor Through Inexpensive Solution Processed V2O5 Complex Surface Architecture. *Electrochim. Acta* **2017**, *242*, 382−389.
(47) Wepasnick, K. A.; Smith, B. A.; Bitter, J. L.; Howard Fairbrother, D. Chemical and Structural Characterization of Carbon Nanotube Surfaces. *Anal. Bioanal. Chem.* **2010**, *396*, 1003−1014.
(48) Lehman, J. H.; Terrones, M.; Mansfield, E.; Hurst, K. E.; Meunier, V. Evaluating the Characteristics of Multiwall Carbon Nanotubes. *Carbon* **2011**, *49*, 2581−2602.
(49) Dresselhaus, M. S.; Jorio, A.; Souza Filho, A. G.; Saito, R. Defect Characterization in Graphene and Carbon Nanotubes Using Raman Spectroscopy. *Philos. Trans. R. Soc., A* **2010**, *368*, 5355−5377.
(50) Chen, Q.; Li, X.; Zang, X.; Cao, Y.; He, Y.; Li, P.; Wang, K.; Wei, J.; Wu, D.; Zhu, H. Effect of Different Gel Electrolytes on Graphene-Based Solid-State Supercapacitors. *RSC Adv.* **2014**, *4*, 36253−36256.
(51) Conway, B. E. *Electrochemical Supercapacitors: Scientific Fundamentals and Technological Applications*; Springer Science & Business Media, 2013.

https://doi.org/10.1021/acsami.1c12551
ACS Appl. Mater. Interfaces 2021, 13, 56004−56013

(52) Wan, Y.; Wang, X. L.; Liu, S. Y.; Li, Y.; Sun, H.; Wang, Q. Effect of Electrochemical Factors on Formation and Reduction of Silver Oxides. *Int. J. Electrochem. Sci.* **2013**, *8*, 12837−12850.
(53) Zequine, C.; Ranaweera, C. K.; Wang, Z.; Singh, S.; Tripathi, P.; Srivastava, O. N.; Gupta, B. K.; Ramasamy, K.; Kahol, P. K.; Dvornic, P. R.; Gupta, R. K. High Performance and Flexible Supercapacitors Based on Carbonized Bamboo Fibers for Wide Temperature Applications. *Sci. Rep.* **2016**, *6*, 31704.
(54) Wu, M.; Li, Y.; Yao, B.; Chen, J.; Li, C.; Shi, G. A High-Performance Current Collector-Free Flexible In-Plane Micro-Supercapacitor Based on a Highly Conductive Reduced Graphene Oxide Film. *J. Mater. Chem. A* **2016**, *4*, 16213−16218.
(55) Bhujun, B.; Tan, M. T. T.; Shanmugam, A. S. Study of Mixed Ternary Transition Metal Ferrites as Potential Electrodes for Supercapacitor Applications. *Results Phys.* **2017**, *7*, 345−353.
(56) Stoller, M. D.; Ruoff, R. S. Best Practice Methods for Determining an Electrode Material's Performance for Ultracapacitors. *Energy Environ. Sci.* **2010**, *3*, 1294−1301.
(57) Khomenko, V.; Frackowiak, E.; Béguin, F. Determination of the Specific Capacitance of Conducting Polymer/Nanotubes Composite Electrodes Using Different Cell Configurations. *Electrochim. Acta* **2005**, *50*, 2499−2506.
(58) Kakaei, K.; Esrafili, M. D.; Ehsani, A. *Graphene Surfaces: Particles and Catalysts*; Academic Press, 2018; Vol. 27.
(59) Jorcin, J.-B.; Orazem, M. E.; Pébère, N.; Tribollet, B. CPE Analysis by Local Electrochemical Impedance Spectroscopy. *Electrochim. Acta* **2006**, *51*, 1473−1479.
(60) Mei, B.-A.; Munteshari, O.; Lau, J.; Dunn, B.; Pilon, L. Physical Interpretations of Nyquist Plots for EDLC Electrodes and Devices. *J. Phys. Chem. C* **2018**, *122*, 194−206.
(61) Landesfeind, J.; Ebner, M.; Eldiven, A.; Wood, V.; Gasteiger, H. A. Tortuosity of Battery Electrodes: Validation of Impedance-Derived Values and Critical Comparison with 3D Tomography. *J. Electrochem. Soc.* **2018**, *165*, A469.
(62) Wang, C.; Appleby, A. J.; Little, F. E. Comparison of the Electrochemical Impedance Spectroscopy Characteristics of Insertion Electrode Materials Used in Secondary Metal Hydride and Lithium-Ion Electrodes. *J. Electrochem. Soc.* **2001**, *148*, A762−A767.
(63) Purkait, T.; Singh, G.; Kumar, D.; Singh, M.; Dey, R. S. High-Performance Flexible Supercapacitors Based on Electrochemically Tailored Three-Dimensional Reduced Graphene Oxide Networks. *Sci. Rep.* **2018**, *8*, 1−13.
(64) Biswal, M.; Banerjee, A.; Deo, M.; Ogale, S. From Dead Leaves to High Energy Density Supercapacitors. *Energy Environ. Sci.* **2013**, *6*, 1249−1259.
(65) Li, W. C.; Mak, C. L.; Kan, C. W.; Hui, C. Y. Enhancing the Capacitive Performance of a Textile-Based CNT Supercapacitor. *RSC Adv.* **2014**, *4*, 64890−64900.
(66) Gupta, R. K.; Candler, J.; Palchoudhury, S.; Ramasamy, K.; Gupta, B. K. Flexible and High Performance Supercapacitors Based on NiCo 2 O 4 for Wide Temperature Range Applications. *Sci. Rep.* **2015**, *5*, 15265.
(67) Zequine, C.; Ranaweera, C. K.; Wang, Z.; Singh, S.; Tripathi, P.; Srivastava, O. N.; Gupta, B. K.; Ramasamy, K.; Kahol, P. K.; Dvornic, P. R.; Gupta, R. K. High Performance and Flexible Supercapacitors Based on Carbonized Bamboo Fibers for Wide Temperature Applications. *Sci. Rep.* **2016**, *6*, 31704.

https://doi.org/10.1021/acsami.1c12551
ACS Appl. Mater. Interfaces 2021, 13, 56004−56013